J. Fluid Mech. (1993), vol. 254, pp. 323–344

The instability of the steady flow past spheres and disks

By RAMESH NATARAJAN[1] AND ANDREAS ACRIVOS[2]
[1] IBM T. J. Watson Research Center, Yorktown Heights, NY 10598, USA
[2] Levich Institute, City College of New York, New York, NY 10031, USA

(Received 3 August 1992 and in revised form 9 February 1993)

We consider the instability of the steady, axisymmetric base flow past a sphere, and a circular disk (oriented broadside-on to the incoming flow). Finite-element methods are used to compute the steady axisymmetric base flows, and to examine their linear instability to three-dimensional modal perturbations. The numerical results show that for the sphere and the circular disk, the first instability of the base flow is through a regular bifurcation, and the critical Reynolds number (based on the body radius) is 105 for the sphere, and 58.25 for the circular disk. In both cases, the unstable mode is non-axisymmetric with azimuthal wavenumber $m = 1$. These computational results are consistent with previous experimental observations (Magarvey & Bishop 1961*a*, *b*; Nakamura 1976; Willmarth, Hawk & Harvey 1964).

1. Introduction

In the case of a circular cylinder in an uniform external flow, the steady two-dimensional separated flow field at low Reynolds number *Re* (which consists of two symmetric recirculating eddies behind the body) eventually becomes unstable to infinitesimal perturbations at sufficiently large *Re*. The experimental results of Provansal, Mathis & Boyer (1987) and Strykowski & Sreenivasan (1990) indicate that this instability appears as a two-dimensional asymmetric low-frequency oscillatory motion of the wake region downstream from the cylinder. The numerical computations of Jackson (1987) also show a two-dimensional Hopf bifurcation in the branch of steady two-dimensional flows as *Re* is increased, and good agreement is obtained with the experimental values for the critical *Re* and the oscillation frequency at the onset of the instability. This instability is the first in the series of flow transitions as *Re* is increased, which at larger *Re* gives rise to periodic vortex shedding from the cylinder, and the formation of the well-known Kármán vortex street.

For axisymmetric bodies in a uniform external flow, the steady separated flow field at low *Re* consists of an axisymmetric, toroidal recirculation eddy behind the body. This flow also becomes unstable at sufficiently large *Re*, but there is less consensus on the details of the first instability in this case. In this work, we have numerically computed the details of the first instability of the steady axisymmetric flow past two bodies, viz. a sphere and a circular disk (oriented broadside-on to the incoming flow). Our results show a regular bifurcation in the branch of steady axisymmetric solutions as *Re* is increased, with the corresponding unstable mode being non-axisymmetric with azimuthal wavenumber $m = 1$. In addition, this instability appears in the near-eddy separated region of the flow immediately behind the body, rather than in the downstream wake. This is quite different from the analogous result in the two-dimensional case mentioned above, but is consistent with the experimental observations in these flows geometries (Magarvey & Bishop 1961*a*, *b*; Nakamura 1976; Willmarth, Hawk & Harvey 1964). In this paper these aspects are discussed, and a comparison to the previous relevant computational work (Kim & Pearlstein 1990) is carried out in the concluding section.

The outline of this paper is as follows. In §2, we describe the problem geometry, as well as the governing equations for the steady axisymmetric base flow, and for the evolution of small-amplitude perturbations to this base flow. In §3, we outline the mesh generation procedure. Section 4 contains the numerical results for the steady flow calculations (including the derivation of appropriate inflow and outflow boundary conditions for this problem). Section 5 describes the numerical methods used for computing the stability-determining eigenvalues from the perturbation equations, and presents the results of the stability analysis. Finally, as mentioned above, §6 compares our computational results with the relevant experimental and numerical work in this area.

2. Problem formulation

The incompressible Navier–Stokes equations are non-dimensionalized with the radius of the body as lengthscale, and the magnitude of the uniform upstream flow as the velocity scale, to obtain

$$\frac{\partial \tilde{\boldsymbol{u}}}{\partial t}+\tilde{\boldsymbol{u}}\cdot\nabla\tilde{\boldsymbol{u}}+\nabla\tilde{p}-Re^{-1}\nabla\cdot(\nabla\tilde{\boldsymbol{u}})=0, \quad \nabla\cdot\tilde{\boldsymbol{u}}=0, \tag{2.1}$$

where $\tilde{\boldsymbol{u}}(r,\theta,z,t)$ is the fluid velocity with components $\{\tilde{u}_r,\tilde{u}_\theta,\tilde{u}_z\}$ in cylindrical coordinates, and $\tilde{p}(r,\theta,z,t)$ is the pressure.

On the body surface denoted by $\mathscr{S}_1$, the usual no-slip velocity boundary condition is used. For computational convenience, the body is assumed to be on the axis of an enclosing cylindrical tube of radius $a \gg 1$ (whose surface is denoted as $\mathscr{S}_2$). The resulting geometry is shown schematically in figure 1 for the sphere. For sufficiently large a, this outer cylindrical surface is shown to have little influence on computational results (particularly for the relatively moderate values of Re of interest to us). Furthermore, for the computation of the base-flow solution in §4, the normal velocity and tangential vorticity components are taken to be zero on $\mathscr{S}_2$. This inviscid boundary condition ensures that the body surface $\mathscr{S}_1$ is the only source of vorticity, as would be the case for an infinite problem domain without the artificial outer cylindrical boundary.

The steady axisymmetric base flow is denoted by $\{\boldsymbol{U}(r,z),\boldsymbol{P}(r,z)\}$, and satisfies the equations

$$\boldsymbol{U}\cdot\nabla\boldsymbol{U}+\nabla P-Re^{-1}\nabla\cdot(\nabla\boldsymbol{U})=0, \quad \nabla\cdot\boldsymbol{U}=0, \tag{2.2}$$

with $\boldsymbol{U}=0$ on $\mathscr{S}_1$. The stability of this base flow is examined by considering small non-axisymmetric perturbations, denoted by $\{\boldsymbol{u}(r,\theta,z,t),p(r,\theta,z,t)\}$, which satisfy the linearized perturbation equations

$$\frac{\partial \boldsymbol{u}}{\partial t}+\boldsymbol{U}\cdot\nabla\boldsymbol{u}+\boldsymbol{u}\cdot\nabla\boldsymbol{U}+\nabla p-Re^{-1}\nabla\cdot(\nabla\boldsymbol{u})=0, \quad \nabla\cdot\boldsymbol{u}=0, \tag{2.3}$$

with $\boldsymbol{u}=0$ on $\mathscr{S}_1$. The details of the remaining boundary conditions are discussed at the appropriate place in §§4 and 5 below.

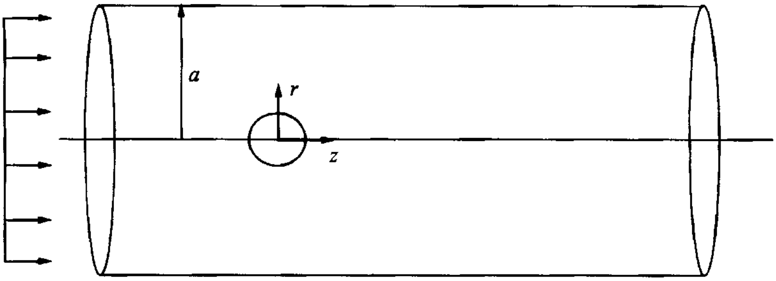

FIGURE 1. Schematic of problem geometry (for flow past a sphere).

3. Mesh generation

The solution of (2.2) and (2.3) requires the generation of two-dimensional grids in the (r, z)-plane, for the region exterior to the body bounded by the lines $r = 0$ and $r = a$, for $-\infty \leqslant z \leqslant \infty$. For convenience in grid generation, this region is conformally mapped to the infinite uniform channel $0 \leqslant R \leqslant A$, $-\infty \leqslant Z \leqslant +\infty$, where (R, Z) denote the coordinates in the mapped domain. Appropriate closed-form expressions for these conformal trnsformations are given in Fornberg (1991), and Natarajan, Fornberg & Acrivos (1993), which can be directly used for the case of the sphere and circular disk respectively.

In order to obtain a finite domain $\mathscr{V}$ for computational purposes, this infinite channel is truncated to the finite region $0 \leqslant R \leqslant A$, $Z_I \leqslant Z \leqslant Z_O$. On this domain, a graded Cartesian product mesh consisting of $N_r \times N_z$ points is generated, and this graded mesh when transformed back to the original (r, z) domain provides a high density of mesh points in the regions where large gradients in the flow solution are expected (particularly in the attached and separated boundary-layer regions, and in the trailing wake). Typical examples of the resulting computational grids are shown in figure 2(*a*) for the sphere, and in figure 2(*b*) for the circular disk. For the circular disk, there is a singularity in the vorticity field at the edge. The mesh generation procedure automatically provides a clustering of mesh points in the neighbourhood of this edge, which is very helpful in resolving the large solution gradients that are expected there.

The boundary lines $Z = Z_I < 0$ and $Z = Z_O > 0$ in the mapped domain are transformed back into the flow inflow and outflow boundaries in the original (r, z) domain, and the corresponding surfaces are denoted by $\mathscr{S}_I$ and $\mathscr{S}_O$ respectively. The magnitudes of Z_I and Z_O should be chosen sufficiently large to capture all the essential details of the flow, whose variations occur primarily on the body scale and near wake. In this context, the specialized asymptotic inflow and outflow boundary conditions for the steady flow problem (described in §4) allow these boundary surfaces to be located closer to the body than would otherwise be possible, and therefore considerably reduce the computational effort required to obtain an accurately resolved solution on the body scale.

4. Stationary problem

In order to solve (2.2), the steady velocity and pressure fields are expanded in the form

$$U = \begin{bmatrix} U_r \\ U_z \end{bmatrix} = \sum_{i=1}^{N} \begin{bmatrix} U_{r,i} \\ U_{z,i} \end{bmatrix} \phi_i(r, z), \quad P = \sum_{i=1}^{M} P_i \chi_i(r, z), \tag{4.1}$$

where $\{U_{r,i}, U_{z,i}, P_i\}$ are the unknown nodal values, and ϕ_i, χ_i are respectively piecewise-continuous biquadratic and bilinear basis functions. The discretization uses

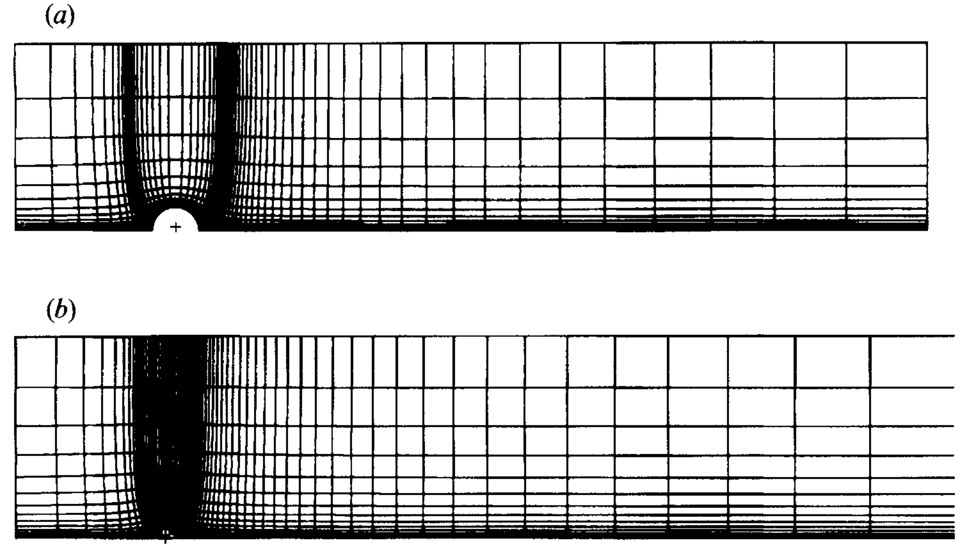

FIGURE 2. Computational mesh M1 (see §4) generated as described in §3. Grid lines in the (r, z)-plane for (a) the sphere, and (b) the circular disk. For clarity, only every second grid line is displayed.

the Taylor–Hood isoparametric quadrangular element (Cuvelier, Segal & van Steenhoven 1986; Gunzburger 1989). Therefore, with the mesh parameters given in §2 (and taking N_r and N_z to be odd), we have $N = N_r \times N_z$ and $M = \frac{1}{2}(N_r+1) \times \frac{1}{2}(N_z+1)$.

After substituting (4.1) in (2.2), and using Galerkin's method followed by an integration by parts (Gunzburger 1989), we obtain

$$\int_{\mathscr{V}} [\boldsymbol{U}\cdot\nabla \boldsymbol{U}\cdot\phi_i \boldsymbol{e}_k - P\nabla\cdot(\phi_i \boldsymbol{e}_k) + Re^{-1}(\nabla \boldsymbol{U})^T : \nabla(\phi_i \boldsymbol{e}_k)]\,\mathrm{d}V$$

$$+\int_{\mathscr{S}} [P\boldsymbol{n}\cdot\phi_i \boldsymbol{e}_k - Re^{-1}\nabla \boldsymbol{U}\cdot\phi_i \boldsymbol{e}_k\cdot \boldsymbol{n}]\,\mathrm{d}S = 0 \quad \text{for} \quad i = 1, N; \quad \boldsymbol{e}_k = \boldsymbol{e}_r, \boldsymbol{e}_z, \qquad (4.2)$$

$$\int_{\mathscr{V}} (\nabla\cdot \boldsymbol{U})\chi_i\,\mathrm{d}V = 0 \quad \text{for} \quad i = 1, M, \qquad (4.3)$$

where $\boldsymbol{n} = n_r \boldsymbol{e}_r + n_z \boldsymbol{e}_z$ is the outward directed normal to the boundary surface $\mathscr{S}$ (where $\mathscr{S} = \mathscr{S}_1 \cup \mathscr{S}_2 \cup \mathscr{S}_I \cup \mathscr{S}_O$). In component form, (4.2)–(4.3) can be written as

$$\int_{\mathscr{V}} \left[\left(U_r\frac{\partial U_r}{\partial r} + U_z\frac{\partial U_r}{\partial z}\right)\phi_i - P\frac{1}{r}\frac{\partial}{\partial r}(r\phi_i) + Re^{-1}\left(\frac{\partial U_r}{\partial r}\frac{\partial \phi_i}{\partial r} + \frac{\partial U_r}{\partial z}\frac{\partial \phi_i}{\partial z} + \frac{U_r\phi_i}{r^2}\right)\right]\mathrm{d}V$$

$$+\int_{\mathscr{S}}\left[Pn_r\phi_i - Re^{-1}\left(\frac{\partial U_r}{\partial r}n_r + \frac{\partial U_r}{\partial z}n_z\right)\phi_i\right]\mathrm{d}S = 0 \quad \text{for} \quad i = 1, N, \qquad (4.4)$$

$$\int_{\mathscr{V}} \left[\left(U_r\frac{\partial U_z}{\partial r} + U_z\frac{\partial U_z}{\partial z}\right)\phi_i - P\frac{\partial \phi_i}{\partial z} + Re^{-1}\left(\frac{\partial U_z}{\partial r}\frac{\partial \phi_i}{\partial r} + \frac{\partial U_z}{\partial z}\frac{\partial \phi_i}{\partial z}\right)\right]\mathrm{d}V$$

$$+\int_{\mathscr{S}}\left[Pn_z\phi_i - Re^{-1}\left(\frac{\partial U_z}{\partial r}n_r + \frac{\partial U_z}{\partial z}n_z\right)\phi_i\right]\mathrm{d}S = 0 \quad \text{for} \quad i = 1, N, \qquad (4.5)$$

$$\int_{\mathscr{V}}\left[\frac{1}{r}\frac{\partial}{\partial r}(rU_r) + \frac{\partial U_z}{\partial z}\right]\chi_i\,\mathrm{d}V = 0 \quad \text{for} \quad i = 1, M. \qquad (4.6)$$

The set (4.4)–(4.5) is subject to the no-slip boundary condition $U_r = U_z = 0$ on $\mathscr{S}_1$ and the inviscid boundary condition $U_r = \partial U_z/\partial r = 0$ on $\mathscr{S}_2$. The inflow and outflow boundary conditions are implemented by adapting the techniques in Natarajan *et al.* (1993) to the present problem. We note, therefore, that sufficiently far upstream and downstream from the body, the steady flow is only slightly disturbed from the uniform free stream, and can be described by the Oseen linearization of the Navier–Stokes equations. For the axisymmetric flow, we have the stream function ψ (where $rU_r = -\partial\psi/\partial z, rU_z = \partial\psi/\partial r$) and the vorticity $\omega = \partial U_r/\partial z - \partial U_z/\partial r$. In the far field, we can write $\psi = \frac{1}{2}r^2 + \hat{\psi}$, $\omega = \hat{\omega}$, in terms of which the linearized Oseen equations are given by

$$\frac{\partial}{\partial r}\frac{1}{r}\frac{\partial}{\partial r}(r\hat{\omega}) + \frac{\partial^2 \hat{\omega}}{\partial z^2} = Re\frac{\partial \hat{\omega}}{\partial z}, \tag{4.7}$$

$$r\frac{\partial}{\partial r}\frac{1}{r}\frac{\partial \hat{\psi}}{\partial r} + \frac{\partial^2 \hat{\psi}}{\partial z^2} = -r\hat{\omega}. \tag{4.8}$$

The set (4.7)–(4.8) has an infinite number of eigenmodes satisfying the condition of vanishing normal velocity component at $r = 0$ and $r = a$. These are of the form

$$\hat{\psi}_n = (A_n \mathrm{e}^{\mu_n^\pm z} + B_n \mathrm{e}^{\lambda_n^\pm z})\, rJ_1(k_n r), \quad \hat{\omega}_n = -Re\, B_n \mathrm{e}^{\lambda_n^\pm z} rJ_1(k_n r), \tag{4.9}$$

where k_n is the nth root of $J_1(ka) = 0$, J_1 being the Bessel function of order 1, and

$$\mu_n^\pm = \pm k_n, \quad \lambda_n^\pm = \tfrac{1}{2}[Re \pm (Re^2 + 4k_n^2)^{\frac{1}{2}}]. \tag{4.10}$$

Here, the quantities $\mu^\pm$ and $\lambda^\pm$ correspond to the spatial growth (or decay) rates of the irrotational and rotational modes respectively. From physical considerations, it is clear that the growing modes in the upstream and downstream directions must be excluded from the solution. In addition, sufficiently far upstream or downstream the solution will be dominated by the leading-order decaying eigenmode in (4.9). For example, in the upstream direction the rotational modes decay rapidly, and if $\mathscr{S}_I$ is located sufficiently far away the flow is essentially dominated by the leading-order irrotational eigenmode, and we have on this boundary

$$\frac{\partial U_r}{\partial r} \approx -\mu_1^+(U_z - 1) - \frac{U_r}{r}, \quad \frac{\partial U_r}{\partial z} \approx \mu_1^+ U_r, \quad \frac{\partial U_z}{\partial r} \approx \mu_1^+ U_r,$$

$$\frac{\partial U_z}{\partial z} \approx \mu_1^+(U_z - 1), \quad P \approx -(U_z - 1),$$

in which the pressure far upstream ($z \rightarrow -\infty$) has been set to zero. The surface integral in (4.4) on $\mathscr{S}_I$ then becomes

$$\int_{\mathscr{S}_I}\left[Pn_r\phi_i - Re^{-1}\left(\frac{\partial U_r}{\partial r}n_r + \frac{\partial U_r}{\partial z}n_z\right)\phi_i\right]\mathrm{d}S$$

$$\approx \int_{\mathscr{S}_I}\left[(n_r - Re^{-1}\mu_1^+ n_r) + Re^{-1}\left(\frac{n_r}{r} + \mu_1^+ n_z\right)U_r + (-n_r + Re^{-1}\mu_1^+ n_r)\,U_z\right]\phi_i\,\mathrm{d}S. \tag{4.11}$$

In contrast, the irrotational modes decay fairly rapidly in the downstream direction, and the far-field solution is eventually dominated by the leading rotational mode. Therefore, in the same way, if $\mathscr{S}_O$ is located sufficiently far away, we have

$$\frac{\partial U_r}{\partial r} \approx -\lambda_1^-(U_z - 1) - \frac{U_r}{r}, \quad \frac{\partial U_r}{\partial z} \approx \lambda_1^- U_r, \quad \frac{\partial U_z}{\partial r} \approx \lambda_1^- U_r,$$

$$\frac{\partial U_z}{\partial z} \approx \lambda_1^-(U_z - 1), \quad P \approx \Delta,$$

where Δ denotes the overall pressure difference ($\Delta \leqslant 0$) between the far upstream and downstream regions. The magnitude of Δ is unknown (except in the case $a \rightarrow \infty$, when $\Delta \rightarrow 0$), and as described below this quantity must also be determined as part of the overall solution procedure. The surface integral in (4.4) on $\mathscr{S}_O$ then becomes

$$\int_{\mathscr{S}_O} \left[P n_r \phi_i - Re^{-1} \left(\frac{\partial U_r}{\partial r} n_r + \frac{\partial U_r}{\partial z} n_z \right) \phi_i \right] \mathrm{d}S$$

$$\approx \int_{\mathscr{S}_O} \left[(\Delta - Re^{-1} \lambda_1^-) n_r + Re^{-1} \left(\frac{n_r}{r} + \lambda_1^- n_z \right) U_r + Re^{-1} \lambda_1^- n_r U_z \right] \phi_i \, \mathrm{d}S. \tag{4.12}$$

The corresponding surface integrals in (4.5) are also transformed in a similar fashion, and these details are omitted here for brevity. Finally, the extra condition for determining Δ is obtained by noting that the overall pressure drop should be consistent with global mass flux conservation, i.e. the condition

$$\int_{\mathscr{S}_O} [U_r n_r + U_z n_z] \, \mathrm{d}S = \tfrac{1}{2} a^2 \tag{4.13}$$

must be imposed on the computed flow solution. The condition (4.13), along with (4.6) ensures that the mass flux across any cross-sectional surface in the flow domain (including, in particular, the inlet surface $\mathscr{S}_I$) is equal the value πa^2 corresponding to the uniform flow at $z \rightarrow -\infty$.

The discrete form of (4.4)–(4.6) and (4.13) is obtained by evaluating the various integrals elementwise using a twelve-point Gaussian quadrature rule. Let X denote a vector of length $2N + M$, consisting of the velocity and pressure nodal unknowns. Then the combined system of equations (4.4)–(4.6) along with (4.13) can be solved by the quadratically convergent Newton iteration

$$\begin{bmatrix} \nabla_X \boldsymbol{R}_1 & \nabla_\Delta \boldsymbol{R}_1 \\ \nabla_X R_2 & 0 \end{bmatrix} \begin{bmatrix} \delta X^n \\ \delta \Delta^n \end{bmatrix} = - \begin{bmatrix} \boldsymbol{R}_1(X^n, \Delta^n) \\ R_2(X^n) \end{bmatrix}, \tag{4.14}$$

starting from a suitable initial guess, until the desired convergence is obtained. In (4.14), $\boldsymbol{R}_1$ and R_2 are the discrete residual equations corresponding to (4.4)–(4.6) and (4.13) respectively, and δX^n and $\delta \Delta^n$ are the updates at each iteration step. An efficient numerical procedure for (4.14) is to first solve for Y_1 and Y_2 from

$$[\nabla_X \boldsymbol{R}_1] \, Y_1 = -\nabla_\Delta \boldsymbol{R}_1, \quad [\nabla_X \boldsymbol{R}_1] \, Y_2 = -\boldsymbol{R}_1. \tag{4.15}$$

Following this, the required solution updates are easily obtained from

$$\delta \Delta^n = (R_2 - \nabla_X R_2 \cdot Y_2)/(\nabla_X R_2 \cdot Y_2), \quad \delta X^n = Y_2 + (\delta \Delta^n) \, Y_1. \tag{4.16}$$

In practice, these iterations were terminated when the maximum pointwise value of the discrete residual dropped below 10^{-12} in magnitude. The resulting solution was then used as a good initial guess for the convergence of the Newton iteration at a larger value of *Re*.

The solution procedure outlined in (4.15)–(4.16) is more economical than the direct solution of (4.14) because the matrix $\nabla_X \boldsymbol{R}_1$ in (4.15) is banded for an appropriate lexicographical ordering of the grid points and unknowns in the finite-element mesh, whereas the extended matrix in (4.14) does not have this useful property. The required

					Storage requirement	
Label	Mesh	Z_I	Z_O	a	steady problem	stability problem
Location of computational boundaries						
L1	135 × 37	−2.5	20	8	48 MB	394 MB
L2	179 × 37	−7.5	40	8	63 MB	—
L3	157 × 45	−5.0	30	12	81 MB	—
Mesh refinement						
M1	135 × 29	−5.0	30	8	24 MB	246 MB
M2	157 × 37	−5.0	30	8	56 MB	459 MB
M3	179 × 45	−5.0	30	8	93 MB	—

TABLE 1. Summary of computational mesh characteristics

band LU factorization and triangular solves in (4.15) are performed using the DGBFA/DGBSL sequence in the LINPACK subroutine library.

For the stability calculations in §5, we are primarily interested in obtaining accurate steady base-flow solutions in the range $80 \leqslant Re \leqslant 120$ for the sphere, and $50 \leqslant Re \leqslant 70$ for the circular disk. The flow quantities used to monitor convergence are the separated eddy length L, the stream function magnitude at the eddy centre ψ_c, and the drag coefficient c_d. The drag coefficient for the sphere is computed from

$$c_d = 4\int_{-1}^{+1}\left[\left(-P+2Re^{-1}\frac{\partial U_z}{\partial z}\right)z+Re^{-1}\left(\frac{\partial U_z}{\partial r}+\frac{\partial U_z}{\partial r}\right)r\right]_{r=(1-z^2)^{\frac{1}{2}}}\mathrm{d}z, \tag{4.17}$$

and for the circular disk from

$$c_d = 4\int_0^1 [P|_{z=0^+}-P|_{z=0^-}]\,r\,\mathrm{d}r. \tag{4.18}$$

Various tests were performed, as described below, to check the convergence of the numerical procedure, and the overall solution correctness and accuracy.

Table 1 shows three meshes L1, L2 and L3, which were used to study the effect of varying the location of the (artificially imposed) exterior boundaries on the solution accuracy. The extent of the inflow and outflow boundaries in L2 is larger by a factor of 2 than L1. In L3, these boundaries are located at the average of L1 and L2, while the extent of the radial boundary is increased by a factor of 1.5. In all cases, the density and distribution of mesh points in the computational grid is kept roughly constant. Table 2(*a*) shows that the primary flow quantities are in excellent agreement on all three meshes.

Table 1 also shows the three meshes M1, M2 and M3 used for the mesh refinement study. The storage requirement for the problem on the finest mesh M3 is roughly twice that for M2, and four times that for M1. Table 2(*b*) shows that the primary flow quantities are in good agreement on all three meshes. Parenthetically, we note that the solution accuracy on the coarsest mesh M1 is somewhat better for the sphere than the circular disk, and this is expected because of the smoother nature of the flow solutions in the former case.

Fornberg (1988) has computed the steady axisymmetric flow past a sphere for Re up to 2500, using finite-difference methods on the vorticity/streamfunction formulation of the Navier–Stokes equations. His results for $Re = 50$ ($L = 2.74$, $c_d = 1.084$), and for

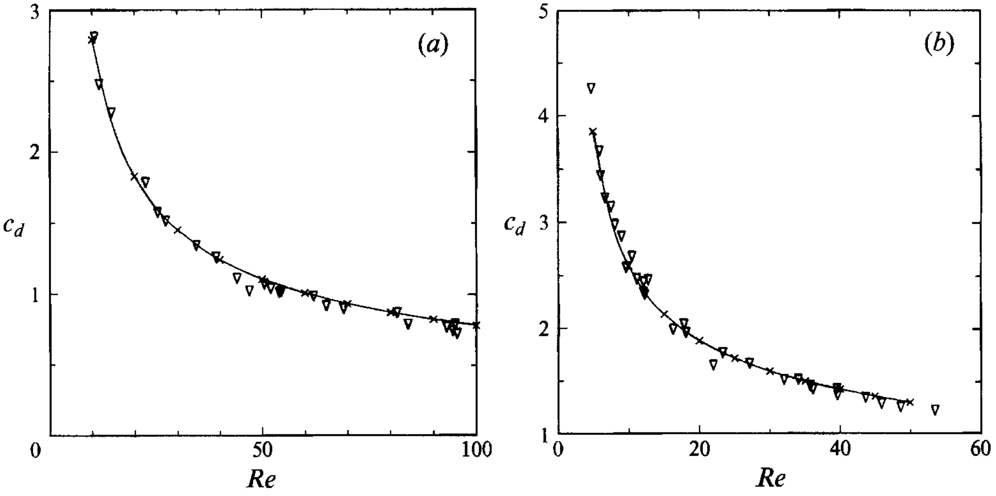

FIGURE 3. Comparison of numerical results for c_d from the steady flow calculations in §3 (denoted by ×, with curve-fitted line also shown). The experimental results (denoted by ▽) are taken from tables in Roos & Willmarth (1971). (a) Sphere; (b) circular disk.

(a)

	L			$-\psi_c$			c_d		
Sphere									
	$Re = 80$	100	120	80	100	120	80	100	120
L1	3.48	3.85	4.14	0.029	0.041	0.054	0.88	0.79	0.72
L2	3.49	3.86	4.15	0.029	0.041	0.054	0.88	0.79	0.72
L3	3.49	3.86	4.15	0.029	0.041	0.054	0.87	0.78	0.71
Circular disk									
	$Re = 50$	60	70	50	60	70	50	60	70
L1	4.07	4.41	4.62	0.178	0.215	0.255	1.31	1.21	1.14
L2	4.08	4.41	4.63	0.178	0.216	0.256	1.31	1.21	1.14
L3	4.09	4.44	4.71	0.175	0.215	0.252	1.27	1.19	1.12

(b)

	L			$-\psi_c$			c_d		
Sphere									
	$Re = 80$	100	120	80	100	120	80	100	120
M1	3.49	3.86	4.13	0.029	0.042	0.054	0.88	0.79	0.72
M2	3.48	3.85	4.13	0.029	0.042	0.054	0.88	0.79	0.72
M3	3.48	3.85	4.14	0.029	0.041	0.054	0.88	0.79	0.72
Circular disk									
	$Re = 50$	60	70	50	60	70	50	60	70
M1	4.07	4.28	4.30	0.175	0.222	0.273	1.29	1.19	1.12
M2	4.05	4.37	4.42	0.177	0.216	0.260	1.31	1.21	1.14
M3	4.07	4.42	4.71	0.177	0.216	0.254	1.31	1.21	1.14

TABLE 2. Convergence studies for steady, base-flow computations: (a) Location of computational boundaries, (b) mesh refinement

$Re = 100$ ($L = 3.87$, $c_d = 0.77$) agree well with our present computations. This good agreement between our results is also found at much larger values of Re, which are however beyond the range of relevance to the stability calculations of the next section, and therefore not discussed further here.

Figures 3(*a*) and 3(*b*) show the good agreement between our numerical results for c_d and the experimental drag measurements for the sphere and circular disk (tabulated in Roos & Willmarth 1971). This comparison is only performed in the relevant range of Re where the experimental flow is also expected to be steady and axisymmetric.

In summary, the various tests above confirm the correctness and accuracy of the steady base-flow computations. Finally, some representative stream function and vorticity contour results are shown in figures 4(*a*) and 4(*b*). In each case, the results shown bracket the critical value Re_1 at which the corresponding axisymmetric flow first becomes unstable (as shown in the next section).

5. Stability problem

Since the base flow is axisymmetric, we can expand the perturbed velocity and pressure fields in (2.3) in the form

$$\begin{bmatrix} \boldsymbol{u} \\ p \end{bmatrix} = \sum_{m=-\infty}^{+\infty} \begin{bmatrix} \boldsymbol{u}^{(m)}(r,z) \\ p^{(m)}(r,z) \end{bmatrix} \mathrm{e}^{\sigma_m t + \mathrm{j} m\theta}, \tag{5.1}$$

where $\mathrm{j} = \sqrt{-1}$, m is the azimuthal mode number, and σ_m is the complex-valued growth (or decay) rate of the corresponding mode perturbation. These perturbed fields are physical quantities, and must be real-valued, so that $\boldsymbol{u}^{(-m)} = \overline{\boldsymbol{u}^{(m)}}$, $p^{(-m)} = \overline{p^{(m)}}$, and $\sigma_{-m} = \overline{\sigma_m}$ (the overbar denotes the complex conjugate).

Similar to the procedure in §4 for the discretization of the base flow, we expand $\{\boldsymbol{u}^{(m)}, p^{(m)}\}$ in the form

$$\boldsymbol{u}^{(m)} = \begin{bmatrix} u_r^{(m)} \\ u_\theta^{(m)} \\ u_z^{(m)} \end{bmatrix} = \sum_{i=1}^{N} \begin{bmatrix} u_{r,i}^{(m)} \\ u_{\theta,i}^{(m)} \\ u_{z,i}^{(m)} \end{bmatrix} \phi_i(r,z), \tag{5.2}$$

$$p^{(m)} = \sum_{i=1}^{M} p_i^{(m)} \chi_i(r,z), \tag{5.3}$$

where $\{u_{r,i}^{(m)}, u_{\theta,i}^{(m)}, u_{z,i}^{(m)}, p_i^{(m)}\}$ are the unknown discrete nodal values of the mode perturbation. Substituting into (2.3), using Galerkin's method followed by an integration by parts, we obtain

$$\int_{\mathscr{V}} \left[\left(\frac{\partial \boldsymbol{u}}{\partial t} + \boldsymbol{U} \cdot \nabla \boldsymbol{u} + \boldsymbol{u} \cdot \nabla \boldsymbol{U} \right) \cdot \phi_i \mathrm{e}^{-\mathrm{j}m\theta} \boldsymbol{e}_k - p \nabla \cdot (\phi_i \mathrm{e}^{-\mathrm{j}m\theta} \boldsymbol{e}_k) + Re^{-1} (\nabla \boldsymbol{u})^T : \nabla (\phi_i \mathrm{e}^{-\mathrm{j}m\theta} \boldsymbol{e}_k) \right] \mathrm{d}V$$

$$+ \int_{\mathscr{S}} [p \boldsymbol{n} \cdot \boldsymbol{e}_k - Re^{-1} \nabla \boldsymbol{u} \cdot \boldsymbol{e}_k \cdot \boldsymbol{n}] \phi_i \mathrm{e}^{-\mathrm{j}m\theta} \mathrm{d}S = 0$$

$$\text{for} \quad i = 1, N; \quad m = -\infty, +\infty; \quad \boldsymbol{e}_k = \boldsymbol{e}_r, \boldsymbol{e}_\theta, \boldsymbol{e}_z, \tag{5.4}$$

$$\int_{\mathscr{V}} (\nabla \cdot \boldsymbol{u}) \chi_i \mathrm{e}^{-\mathrm{j}m\theta} \mathrm{d}V = 0 \quad \text{for} \quad i = 1, M; \quad m = -\infty, +\infty. \tag{5.5}$$

The equations (5.4)–(5.5) decouple for each value of m, so that the corresponding superscript on the dependent variables can be omitted without confusion, thereby

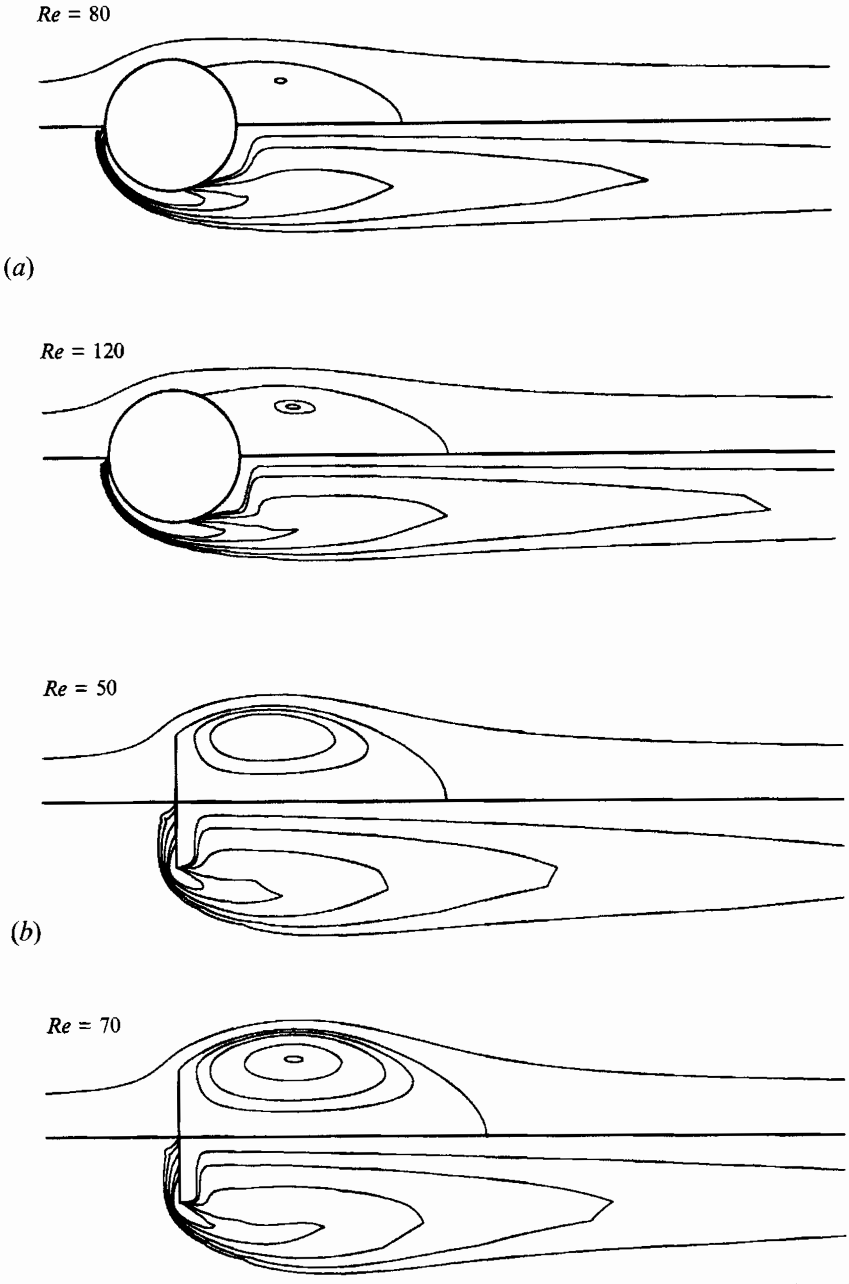

FIGURE 4. Contours of stream function (upper half) and vorticity (lower half) for (*a*) the sphere with $Re = 80$, 120; (*b*) the circular disk with $Re = 50$, 70. Contour values are (0.2, 0, -0.05, -0.1, -0.2, ψ_c) for stream function and (-0.25, -0.5, -1.0, -2.0, -3.0) from vorticity.

considerably simplifying the notation below. Thus, writing out (5.4)–(5.5) in component form, we obtain the following set:

$$\int_{\mathscr{V}}\left[\left(\sigma u_r + U_r\frac{\partial u_r}{\partial r} + u_r\frac{\partial U_r}{\partial r} + U_z\frac{\partial u_r}{\partial z} + u_z\frac{\partial U_r}{\partial z}\right)\phi_i - p\frac{1}{r}\frac{\partial}{\partial r}(r\phi_i)\right.$$

$$\left. + Re^{-1}\left(\frac{\partial u_r}{\partial r}\frac{\partial \phi_i}{\partial r} + \frac{\partial u_r}{\partial z}\frac{\partial \phi_i}{\partial z} + \frac{(m^2+1)}{r^2}u_r\phi_i + \frac{jm}{r^2}u_\theta\phi_i\right)\right]\mathrm{d}V$$

$$+\int_{\mathscr{S}}\left[pn_r\phi_i - Re^{-1}\left(\frac{\partial u_r}{\partial r}n_r + \frac{\partial u_r}{\partial z}n_z\right)\phi_i\right]\mathrm{d}S = 0 \quad \text{for} \quad i = 1, N, \tag{5.6}$$

$$\int_{\mathscr{V}}\left[\left(\sigma u_\theta + U_r\frac{\partial u_\theta}{\partial r} + U_z\frac{\partial u_\theta}{\partial z} + \frac{u_\theta U_r}{r}\right)\phi_i + \frac{jm}{r}p\phi_i\right.$$

$$\left. + Re^{-1}\left(\frac{\partial u_\theta}{\partial r}\frac{\partial \phi_i}{\partial r} + \frac{\partial u_\theta}{\partial z}\frac{\partial \phi_i}{\partial z} + \frac{(m^2-2jm+1)}{r^2}u_\theta\phi_i\right)\right]\mathrm{d}V$$

$$+\int_{\mathscr{S}}\left[-Re^{-1}\left(\frac{\partial u_\theta}{\partial r}n_r + \frac{\partial u_\theta}{\partial z}n_z\right)\phi_i\right]\mathrm{d}S = 0 \quad \text{for} \quad i = 1, N, \tag{5.7}$$

$$\int_{\mathscr{V}}\left[\left(\sigma u_z + U_r\frac{\partial u_z}{\partial r} + u_r\frac{\partial U_z}{\partial r} + U_z\frac{\partial u_z}{\partial z} + u_z\frac{\partial U_r}{\partial z}\right)\phi_i - p\frac{\partial \phi_i}{\partial z}\right.$$

$$\left. + Re^{-1}\left(\frac{\partial u_z}{\partial r}\frac{\partial \phi_i}{\partial r} + \frac{\partial u_z}{\partial z}\frac{\partial \phi_i}{\partial z} + \frac{m^2}{r^2}u_z\phi_i\right)\right]\mathrm{d}V$$

$$+\int_{\mathscr{S}}\left[pn_z\phi_i - Re^{-1}\left(\frac{\partial u_z}{\partial r}n_r + \frac{\partial u_z}{\partial z}n_z\right)\phi_i\right]\mathrm{d}S = 0 \quad \text{for} \quad i = 1, N, \tag{5.8}$$

$$\int_{\mathscr{V}}\left[\frac{1}{r}\frac{\partial}{\partial r}(ru_r) + \frac{jm}{r}u_\theta + \frac{\partial u_z}{\partial z}\right]\chi_i\,\mathrm{d}V = 0 \quad \text{for} \quad i = 1, M. \tag{5.9}$$

The no-slip boundary condition $u_r = u_\theta = u_z = 0$ is used on $\mathscr{S}_1$. On the inflow surface $\mathscr{S}_I$, the velocity perturbation is set to zero. This is justified since even for very large *Re* (when the actual flow may be non-axisymmetric and time-dependent elsewhere), the upstream region of the flow is expected to be inviscid with little deviation there from the corresponding axisymmetric base-flow solution at that value of *Re*. On the surface $\mathscr{S}_2$, the boundary condition $u_r = \partial u_z/\partial r = \partial u_\theta/\partial r$ was used. This is precisely the natural boundary condition on $\mathscr{S}_2$ in (5.7) and (5.8). In practice, we have observed essentially unchanged results with a zero velocity perturbation boundary condition on $\mathscr{S}_2$, and this is to be expected using the same physical reasoning as above for the inflow boundary condition. Similarly, on the surface $\mathscr{S}_O$, we use the appropriate natural boundary conditions in (5.6)–(5.8), i.e. $-p\boldsymbol{n} + Re^{-1}\,\partial\boldsymbol{u}/\partial n = 0$, which is a widely used outflow boundary condition for the Navier–Stokes equations in the finite-element literature (Jackson 1987; Gunzburger 1989; Gresho 1991) although it does not have a specific physical interpretation. The boundary conditions used here are straightforward to implement, and by varying the size of the computational domain, can be shown to provide results of acceptable accuracy. As an aside, we note that the derivation of suitable inflow and outflow boundary conditions for the time-dependent Navier–Stokes equations, or even their linearized form (2.3), paralleling the treatment in §4 for the steady problem, would be a most useful theoretical development. This detailed aspect has not been pursued in the present set of calculations (Hagstrom 1991 and Gresho 1991 provide an entry into the literature on the implementation of outflow boundary conditions for the Navier–Stokes equations).

The discrete form of (5.6)–(5.9) is obtained by evaluating the various integrals elementwise using a twelve-point Gaussian quadrature rule. Let Y denote a vector of length $3N+M$, consisting of the perturbation velocity and pressure unknowns. Then (5.6)–(5.9) can be written as the generalized matrix eigenvalue problem

$$\boldsymbol{A}Y = \sigma \boldsymbol{B}Y, \tag{5.10}$$

where $\boldsymbol{A}$ is a complex-valued, non-symmetric matrix, and $\boldsymbol{B}$ is a real-valued, symmetric matrix. The matrix $\boldsymbol{B}$ is equivalent to copies of the finite-element 'mass' matrix for the discretization, but is singular with M rows in it being identically zero (due to the absence of a time-derivative in the continuity equation). In addition, the homogeneous essential boundary conditions on the discrete perturbation vector Y are directly imposed in the discrete form (5.10), by setting all the entries in the corresponding row of the matrices $\boldsymbol{A}$ and $\boldsymbol{B}$ to zero, except for the diagonal entry in $\boldsymbol{A}$ which is set to unity (this is seen to have the desired effect of forcing the corresponding nodal value in Y to zero).

The linearized stability of the base flow at different Re can be determined from the eigenvalues σ of (5.10). For sufficiently small Re, all eigenvalues have $\mathrm{Re}(\sigma) < 0$ so that the corresponding eigenmodes will decay. There is a critical value Re_c at which the 'leading' eigenvalue (i.e. the eigenvalue with the maximum real part) crosses the imaginary axis into the right half-plane, so that the corresponding eigenmode is linearly unstable. If the corresponding imaginary part of this leading eigenvalue is zero at Re_c, then we have a regular bifurcation to a steady secondary solution. However, if it is non-zero, so that crossing occurs for a complex-conjugate pair of eigenvalues, then we have a Hopf bifurcation to a time-periodic secondary solution, whose frequency at the onset of this instability is determined by the magnitude of the imaginary part of the eigenvalue at this crossing. In either case, the spatial form of the bifurcating solution is determined by the eigenspace of the crossing eigenvalue (or conjugate pair of eigenvalues).

The matrices $\boldsymbol{A}$ and $\boldsymbol{B}$ are banded for an appropriate lexicographic ordering of the grid points and unknowns in the computational mesh. Furthermore, in the present application, only the eigenvalues of (5.10) in the least stable region of the spectrum are of interest. A suitable numerical scheme is described in Natarajan (1992), which exploits the specific characteristics of these stability applications for efficiently performing the relevant eigenvalue computations. Briefly, a shift-and-invert transformation, with a designated complex shift λ, is used to take (5.10) to the form

$$\boldsymbol{K}Z \equiv (\boldsymbol{A}-\lambda\boldsymbol{B})^{-1}\boldsymbol{B}Z = \hat{\sigma}Z, \tag{5.11}$$

which is a standard eigenvalue problem for a complex, non-symmetric matrix $\boldsymbol{K}$, whose eigenvalues $\hat{\sigma}$ are related to those of (5.10) by $\hat{\sigma} = 1/(\sigma-\lambda)$. A restarted, iterative Arnoldi algorithm (Saad 1988) is then used to solve (5.11). The computationally expensive part of this algorithm is the matrix-vector products involving $\boldsymbol{K}$, which can be efficiently carried out without explicitly forming $\boldsymbol{K}$, by first performing the matrix-vector product with $\boldsymbol{B}$, followed by forward and backward solves with the band

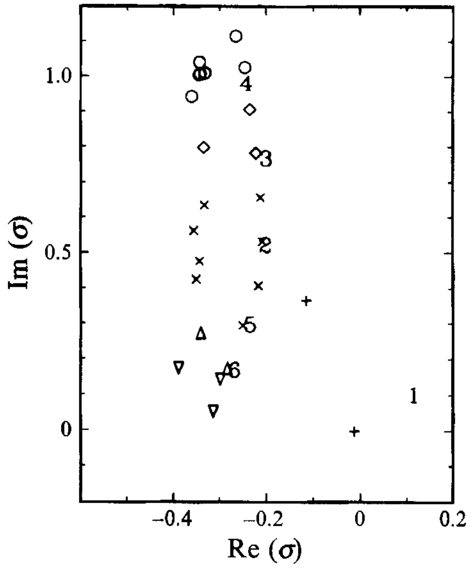

FIGURE 5. Illustration of shift selection procedure and eigenvalue convergence for the case $Re = 100$, $m = 1$ on the mesh M1. The numerals give the location of shifts and their sequence. The symbols are the corresponding converged eigenvalues at each shift denoted by the following sequence (1) +, (2) ×, (3) ◇, (4) ○, (5) △, (6) ▽. In figures 5–7, only the computed eigenvalues with $\mathrm{Im}(\sigma) \geqslant 0$ are shown.

triangular factors of $\boldsymbol{A}-\lambda\boldsymbol{B}$. The complex, band LU factorization and triangular solves required in this procedure are performed using the ZGBFA/ZGBSL routines in the LINPACK library.

In this scheme, the eigenvalues of (5.10) located near the initial shift λ (in the complex plane), are the fastest to converge. In Natarajan (1992), a procedure is described for adaptively generating a sequence of shifts, so that by repeating the Arnoldi procedure at each shift, the progress of the convergence of eigenvalues is effectively biased to the desired least-stable eigenvalues of (5.10). Some features of the present problem allow further computational efficiency to be obtained in the eigenvalue extraction procedure. First, since in practice the complex eigenvalues of (5.10) always appear as conjugate pairs, the computational effort can be confined to obtaining the eigenvalues with $\mathrm{Im}(\sigma) \geqslant 0$. Second, a preliminary idea of the relevant eigenvalue distribution is always apparent from coarse mesh computations or from results obtained at nearby values of Re. With this information at hand, an initial shift can be specified near the leading eigenvalues in the spectrum. Aside from these leading eigenvalues, the remaining details of the spectrum are not particularly relevant to the linear stability arguments. Nevertheless, these details are useful in comparing the computational results obtained on different meshes, and in tracking the changes in the stability spectrum as Re is varied.

Figure 5 illustrates this algorithmic procedure for a typical calculation, in this case for a sphere ($Re = 100$, $m = 1$). Here, the various numerals in the graph are located at the shift values and denote the order of their usage, and the symbols denote the corresponding converged eigenvalues computed at each shift value. The shift values are automatically generated by the algorithm, and are located in the regions of the complex plane where further unconverged eigenvalues might be found. As shown here, the sequence in which these shift values are used is biased towards extracting the least-

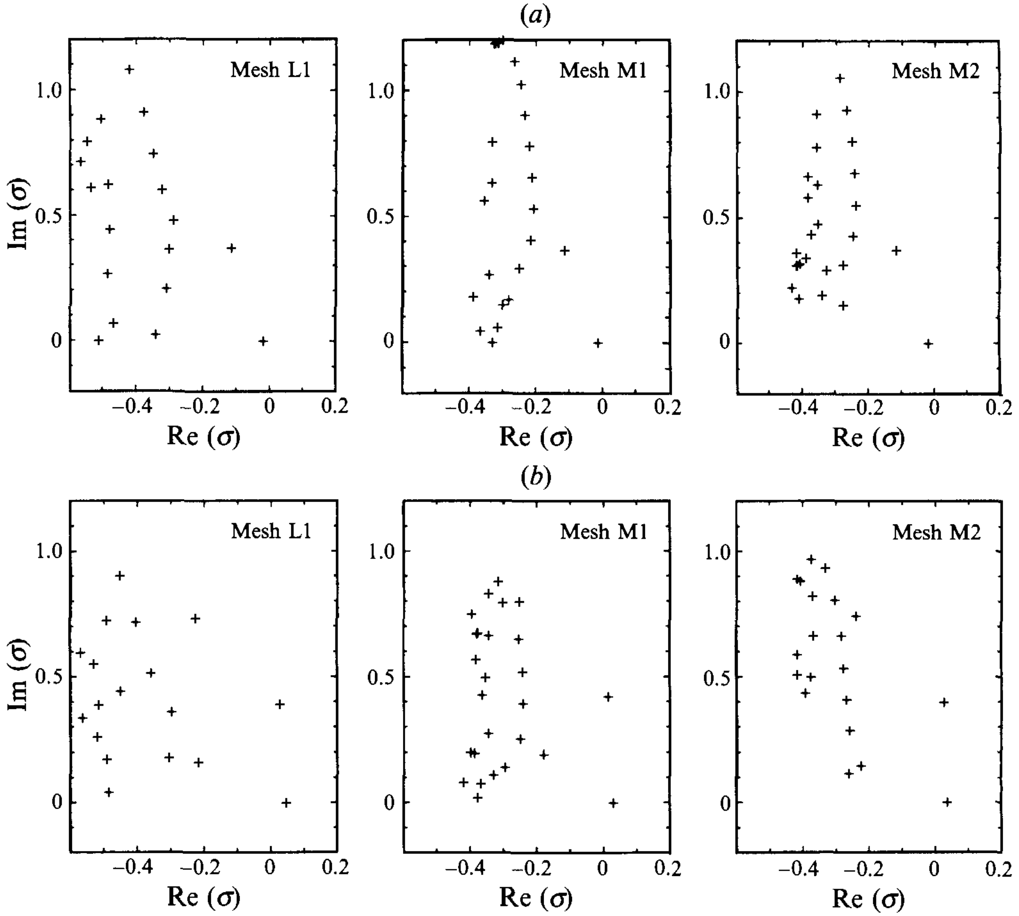

FIGURE 6. Effect of the location of the inflow and outflow boundaries, and the mesh density on the eigenvalue results. For the mode $m = 1$, (*a*) sphere for $Re = 100$, and (*b*) circular disk for $Re = 70$. The two leading eigenvalues have identical values on all three meshes L1, M1 and M2.

stable eigenvalues in the spectrum. In this particular representative run, about 26 eigenvalues were obtained, with an initial Krylov basis set of dimension 70, and a convergence criterion of 10^{-12} in the Arnoldi iterations (see Natarajan 1992). The accuracy of the converged eigenpairs was independently checked by evaluating the residual $\max_i |(A_{ij} - \sigma B_{ij})\, Y_j|$, and this quantity was always less than 10^{-9} for the reported results. More importantly, for the leading few eigenpairs, this residual was generally less than 10^{-12}, so that evey better accuracy is guaranteed for these.

The effect of varying the location of the exterior computational boundaries, and of mesh refinement, is considered by examining the results for the $m = 1$ mode on the meshes L1, M1 and M2. Figures 6(*a*) and 6(*b*) show results for the sphere ($Re = 100$) and circular disk ($Re = 70$). In each case, there are two leading eigenvalues (one real and one complex) which are well separated from the rest of the spectrum, and whose values are essentially identical on all three meshes. Some of the difference in the details of the interior parts of the spectrum from these three meshes is attributable to the automatic shift selection procedure which explores different regions of the spectrum in each case. Aside from this, the interior spectrum for L1 is seen to be noticeably sparser than for M1 and M2. The new eigenvalues appearing in the latter two cases might be

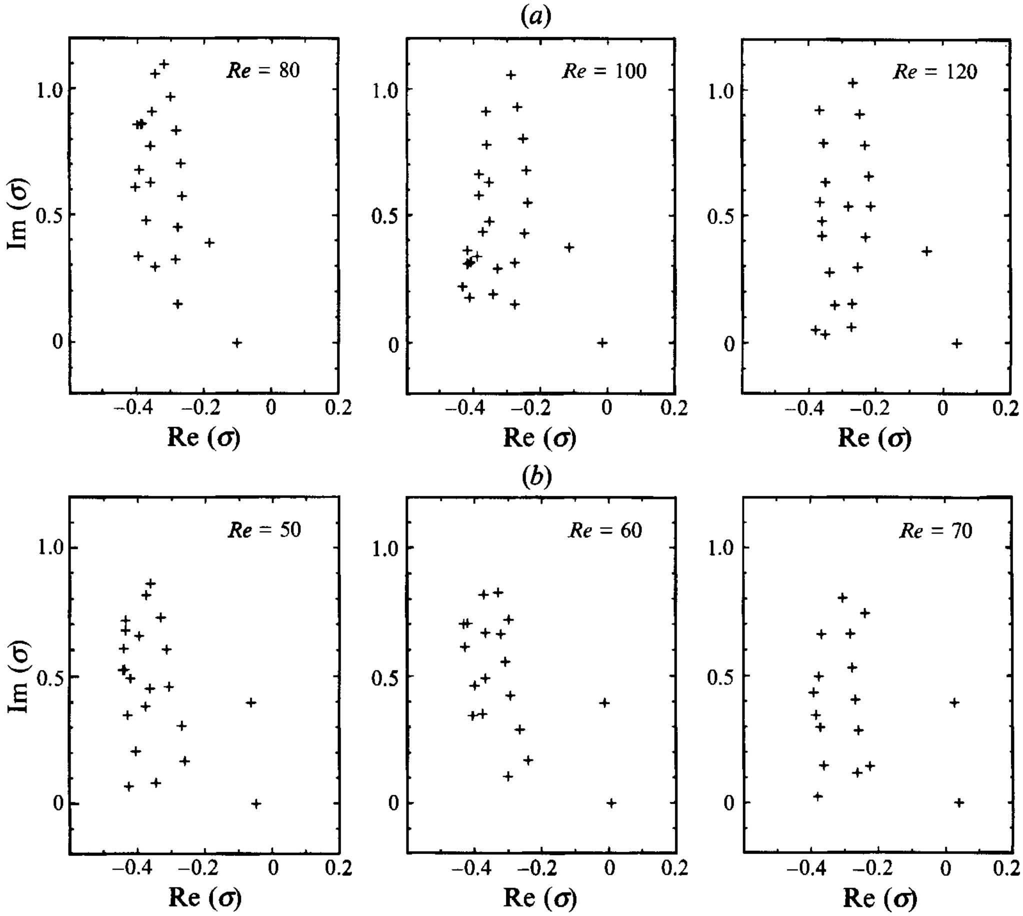

FIGURE 7. Effect of varying *Re* on the eigenvalues for the $m = 1$ mode, in the range where it is unstable. (*a*) Sphere, and (*b*) circular disk. All results on the mesh M2.

associated with any of three causes, viz. the location and the boundary conditions used at the inflow and outflow boundaries (particularly the latter), the details of the flow in the extreme far wake, or the mesh refinement. A cursory examination of some of the eigenfunctions corresponding to these interior eigenvalues does in fact show that their spatial variation is primarily near the outflow boundary outside the wake region, and tends to support the hypothesis that many of these modes do not have any physical implication (and hence would probably be eliminated by the 'right' outflow boundary condition). It is significant that these particular 'spurious' eigenvalues do not show any tendency towards becoming more unstable as *Re* is varied, so that the instability transitions can be ascribed to be entirely a consequence of the flow details on the body scale and near wake.

The variation in the eigenvalue spectrum as a function of *Re* is considered in figure 7(*a*) for the sphere, and figure 7(*b*) for the circular disk. As *Re* is increased from small values, the two leading eigenvalues are seen to move towards the imaginary axis. In each case, the crossing first occurs for the real eigenvalue at Re_1 (which is a regular bifurcation point on the branch of base flows). Some detailed calculations show that $Re_1 = 105$ for the sphere, and 58.25 for the circular disk. Also, in each case, the other

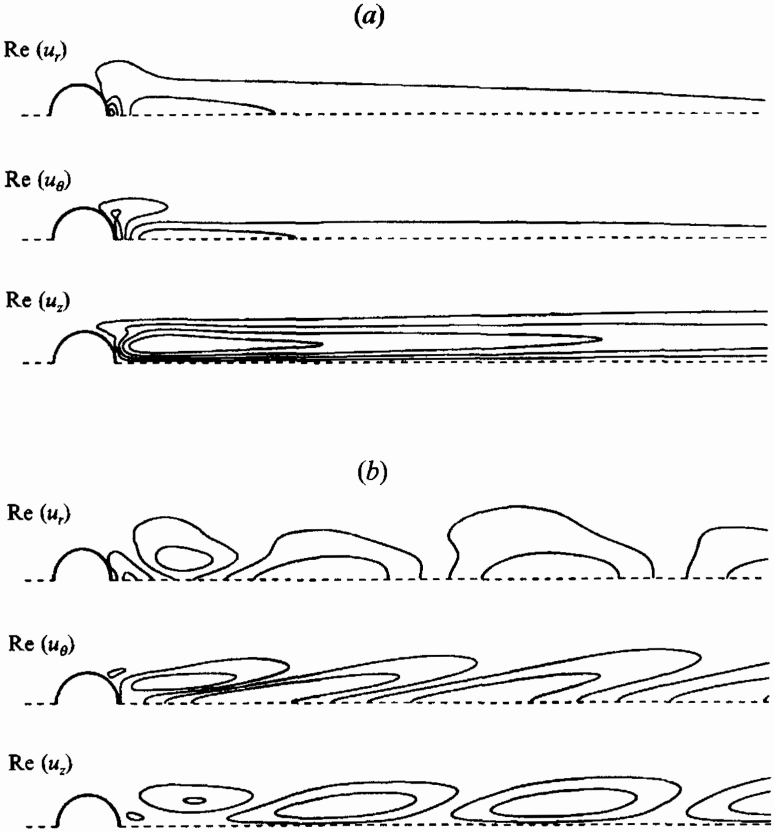

FIGURE 8. Spatial form of the eigenfunctions at the bifurcation points for the sphere. (a) $Re = 105$, (b) $Re = 138.75$.

leading complex eigenvalue also crosses into the right half-plane at a supercritical value Re_2 (which is a Hopf bifurcation point on the now-unstable branch of base flows), with the magnitude of the imaginary part of this crossing eigenvalue being given by Ω_2. Again, detailed computations show $Re_2 = 138.75$, $\Omega_2 = 0.355$ for the sphere, and $Re_2 = 62.8$, $\Omega_2 = 0.395$ for the circular disk.

The spatial form of the unstable eigenvector at the bifurcation points Re_1 and Re_2 is considered in figure 8 for the sphere, and in figure 9 for the circular disk. These are equispaced contour plots of the real parts of $\{u_r, u_\theta, u_z\}$ given in (5.6)–(5.9) for the unstable eigenvector (the corresponding imaginary parts are scaled and normalized differently, but have basically the same structure, and we omit their description here). At both Re_1 and Re_2, the similarity in the results for the sphere and circular disk is quite striking, indicating that these two unstable modes have the same physical origin in the case of both bodies. At Re_1, the variation of the unstable eigenvector is primarily in the near-eddy region of the axisymmetric base flow. At Re_2, however, these variations have the spatially periodic downstream structure that is characteristic of an oscillatory wake instability (see, for example, Jackson 1987 for the case of flow past a cylinder).

On the basis of the experimental results described in §6, we conjecture here that a stable supercritical branch of steady non-axisymmetric flow solutions will bifurcate from the base flow at Re_1. Furthermore, we anticipate that a secondary Hopf bifurcation will occur on this branch at some supercritical value, say $Re_{1,2}$, which will

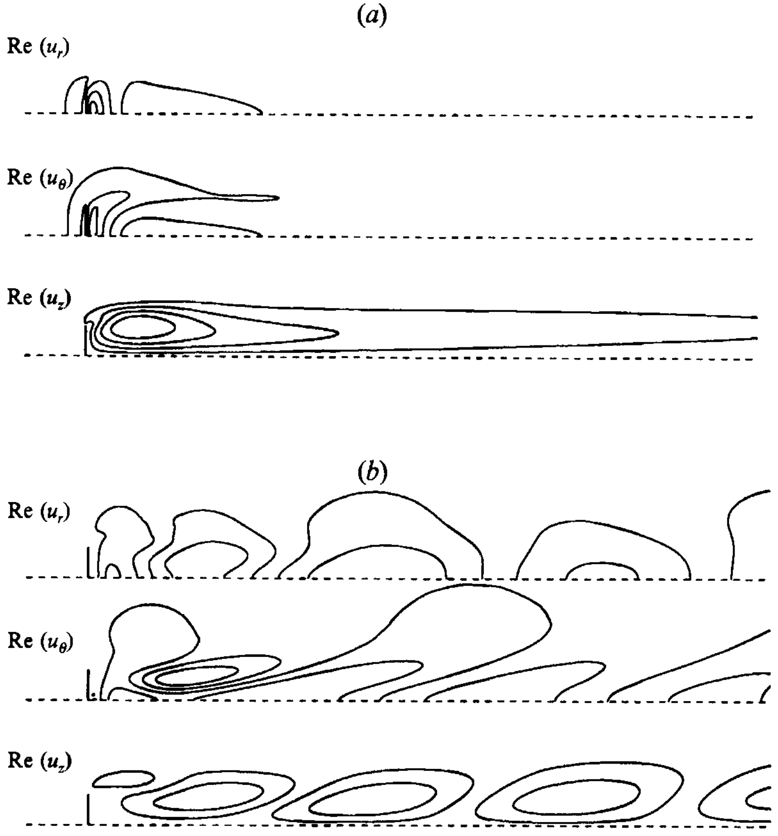

FIGURE 9. Spatial form of the eigenfunctions at the bifurcation points for the circular disk. (*a*) $Re = 58.25$, (*b*) $Re = 62.8$.

correspond to the critical *Re* for onset of time-dependence in the flow field. The unstable mode for this anticipated secondary Hopf bifurcation at $Re_{1,2}$ could be closely related to the mode responsible for the Hopf bifurcation computed here in the branch of base-flow solutions at Re_2. This is reasonable if the amount of non-axisymmetric distortion in the bifurcating steady solution is sufficiently small (particularly in the far-wake region where this particular mode is excited), so that the original branch of base-flow solutions is still a good approximation to the supercritical flow field. This is especially likely for the circular disk since in this case Re_2 is only slightly greater than Re_1. If this scenario is true, then the values Re_2 and Ω_2 provide an estimate for the critical Reynolds number and frequency at the actual onset of time-dependence in the flow field. Further numerical computations are required to confirm all these conjectures, but the required effort lies outside the scope of the present investigation.

Finally, we show the stability spectrum of the other azimuthal modes for a value of $Re > Re_c$, where the $m = 1$ mode is already unstable. Figure 10(*a*) shows the results for the sphere at $Re = 120$, and figure 10(*b*) for the circular disk at $Re = 70$. In the cases $m = 0, 2, 3$ investigated, there was no indication of any potentially unstable eigenvalues for these modes.

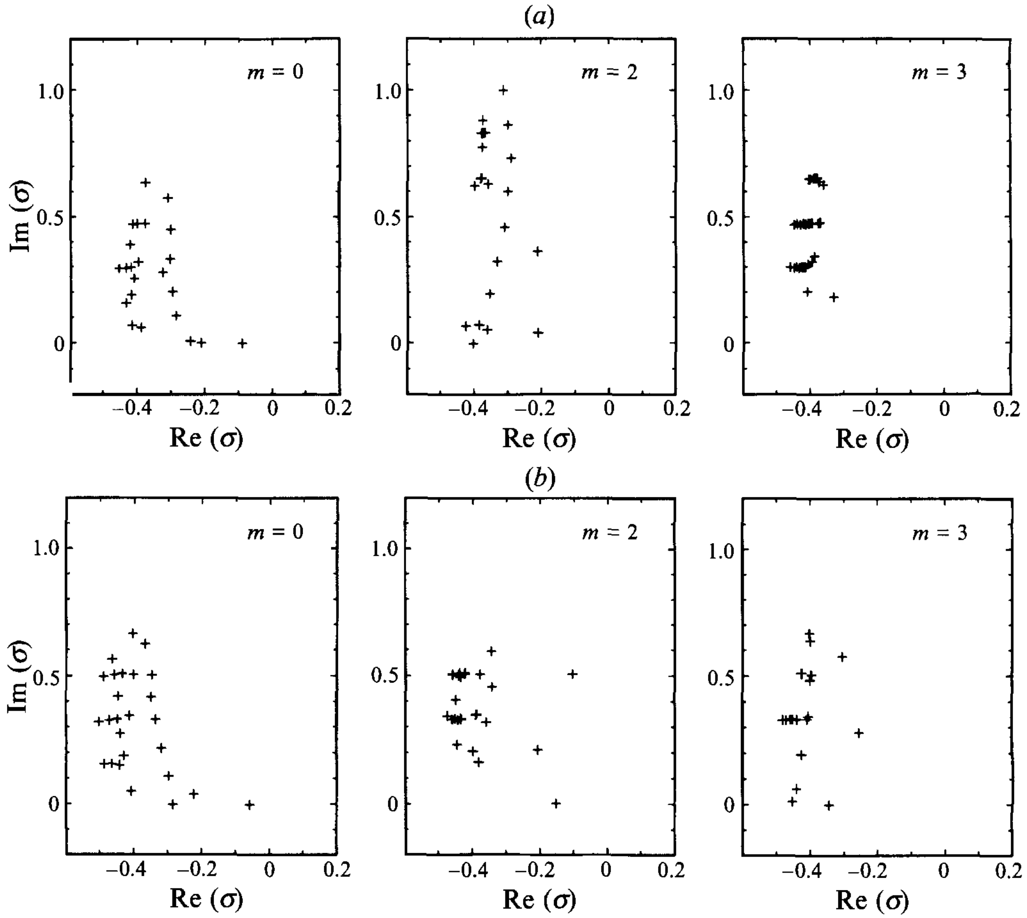

FIGURE 10. Stability spectrum of the azimuthal mode perturbations ($m = 0, 2, 3$) at a value of Re when the primary $m = 1$ mode is already unstable: (*a*) sphere, $Re = 120$, and (*b*) circular disk, $Re = 70$. All results on the mesh M2.

6. Discussion

Kim & Pearlstein (1990) have previously considered the numerical determination of the first instability mode for flow past a sphere, using spectral discretization methods for the base flow and linearized stability equations. They also show that the first unstable mode is non-axisymmetric with azimuthal wavenumber $m = 1$, but their description differs from ours since they report that the onset of the instability is through a Hopf bifurcation at a critical Re of around 87.5. The complicated nature of the numerical problem, and the different computational approaches used in these studies, make it difficult to resolve this discrepancy in a straightforward manner. Nevertheless, there are three particular aspects that would seem to favour our results in this paper. First, our results are more consistent with some experimental observations for flow past a sphere, described further in detail below, which clearly show the existence of stable axisymmetric flow solutions for some range of values of Re greater than their critical value of 87.5. In addition, these experiments also show steady non-axisymmetric flow solutions over another range of Re beyond this, and the existence of these solutions cannot be explained from their results. Second, the decay rates for the stable perturbations reported by Kim & Pearlstein (1990) are systematically seen to have a smaller magnitude than might be expected on physical considerations. For example, in the case $Re = 25$, the least-stable eigenvalue for the mode with azimuthal wavenumber $m = 0$ is reported to have a decay rate around -9.0×10^{-4} (see table 1 in their paper), and this is inconsistent with the expectation that this particular mode should be very strongly damped at such a low value of Re. Third, recent numerical computations in Tomboulides, Orszag & Karniadakis (1993) and Tomboulides (1993) for flow past a sphere, which we briefly describe below, provide a description of this instability that quantitatively confirms many aspects of our results.

Some photographs of the wakes produced by a liquid drop settling in a surrounding immiscible liquid are shown in Magarvey & Bishop (1961*a*, *b*), and Magarvey & Maclatchy (1965). In these experiments, some dye was introduced into a droplet phase, which was then scrubbed from the interface by the flow into the region behind the drop, thereby rendering the structure of the flow in the wake region visible. Their results show that for low Re the flow consists of a toroidal recirculating eddy attached to the rear of the drop, with a single thread of dye in the trailing wake far downstream. At $Re \approx 105$ (where our calculations show the $m = 1$ mode to become unstable), they observed a transition to a steady non-axisymmetric flow with a double thread of dye in the trailing wake. We conjecture that this is the stable solution for supercritical values of Re, and that its spatial form can be obtained from the eigenfunction of the unstable $m = 1$ mode. This is consistent with the experimental results, but its full theoretical justification requires a nonlinear analysis of the stability of the entire class of bifurcating solutions (which consists of arbitrary linear combinations of the unstable $m = 1$ mode superposed with different azimuthal phases). This nonlinear analysis, however, lies outside the scope of the present work.

To emphasize the relevance of the experimental results of Magarvey & Maclatchy (1965) to our numerical calculations, we note that the photographs in that paper show that the liquid drop does not undergo any discernable deformation from the spherical shape, and there is little evidence of any internal circulation within the drop during the motion. This is presumably due to the inhibiting effect of surface-active impurities, which form a rigid film at the liquid–liquid drop interface, and cause the drop to effectively behave as a solid sphere. This reasoning is supported by the fact that Winnikow & Chao (1966), in subsequent experiments with more purified liquid systems, have shown the importance of drop deformation, oscillation, and internal flow circulation, and have observed that, consistent with these experimental differences, the onset of separation and the subsequent instabilities in these systems was delayed to comparatively larger values of Re.

Nakamura (1976), has conducted experiments with falling solid spheres, and has published photographs showing the transition from steady axisymmetric to steady non-axisymmetric flows. He reports that this transition takes place at $Re \approx 95$, with steady single-threaded as well as double-threaded wake flows for some range of values of $Re > 95$.

Insofar as the onset of time-dependent motion in the flow is concerned, Magarvey & Maclatchy (1961*a*, *b*) have observed wavy motions far downstream in the double-threaded wake flow as Re was increased beyond 135. Similarly, a time-dependent wavy motion has also been observed for $Re \approx 135$ in the wake of freely falling solid spheres (Goldburg & Florsheim 1966). We note that these values are close to $Re_2 = 138.5$ (see remarks below, and at the end of §5). As mentioned earlier, it would follow that the onset of time-dependence in the flow past a sphere (and equivalently, for flow past a circular disk) is through a Hopf bifurcation in the secondary branch of bifurcating steady, non-axisymmetric transitional flows. This is in distinct contrast to the case of flow past a circular cylinder where the onset of time-dependence is directly through a Hopf bifurcation in the branch of base-flow solutions. At larger values of *Re*, this time-dependent wake instability eventually leads to an asymmetric vortex shedding in the form of a double row of vortex loops or rings. Further details of the high-*Re* flow in the vortex shedding regime for flow past spheres can be found in Achenbach (1974), Taneda (1978) and Sakamoto & Haniu (1990).

In the case of circular disks, there are few rigorous experimental data that are relevant to the instability of the base flow. However, Willmarth *et al.* (1963) describe experiments with freely falling circular disks which are initially dropped in a 'broadside-on' orientation. For $Re < 50$, the falling disks retained this particular orientation, and a steady axisymmetric recirculating wake was clearly visible behind the disk. For larger values of *Re*, the disks fell erratically with translational and tumbling motions. This behaviour is consistent with the computed instability of the base axisymmetric flow in this range of *Re*, and is also consistent with our expectation that for circular disks, the flow will become time-dependent at a supercritical value of *Re* only slightly beyond that for the first instability.

The experimental results discussed above primarily concern freely falling spheres (including rigid drops) and circular disks, for which there is a mutual interaction between the body and the flow field around it. For example, the non-axisymmetric flow field at supercritical values of *Re* can lead to sideways forces and the lateral drifting of freely falling spheres (although in this case, the onset of the primary instability itself should not be affected). For circular disks, the effect of orientational perturbations during descent can interact with and modify the purely fluid dynamical instability studied here. The general agreement of the experiments with our computational results indicates that these interaction effects are likely to be moderate in practice, although this issue certainly deserves further investigation. Other rigorous experimental investigations with rigidly anchored spheres (see the extensive reviews in Kim & Pearlstein 1990; Sakamoto & Haniu 1990) unfortunately do not provide sufficient details of the near-eddy wake flow structure in the relevant range of *Re* for comparison to our computations.

The instabilities described here have been studied independently, using a different but complementary approach, by Tomboulides *et al.* (1993) and Tomboulides (1993). This approach is based on a time-dependent code developed for studying the fully three-dimensional flow past a sphere. In this code, the dependent variables are Fourier-decomposed in the azimuthal direction, and expanded on a spectral element basis in the (r, z)-plane. By 'turning off' the non-axisymmetric ($m \neq 0$) Fourier modes, they compute steady axisymmetric flow solutions (which are identical to our base flow solutions for the sphere). Then with the non-axisymmetric modes 'turned on', small perturbations are introduced and allowed to evolve in time. One such experiment at $Re = 125$, showed the $m = 1$ component of the azimuthal velocity in the wake to initially grow exponentially and then eventually saturate at a new steady state. A background subdominant mode was also identified that decayed after a few oscillations. The structure of the dominant growing mode and the estimated growth rates of both the growing dominant and decaying subdominant mode are in close agreement with our eigenvalue computations. Another such experiment at $Re = 150$ shows initially in the time evolution a dominant exponentially growing mode, and a subdominant oscillatory but exponentially growing mode. The estimated growth rates in this case are also in close quantitative agreement with our eigenvalue computations. It should be noted that their use of a time-dependent code in this fashion has the advantage that the evolution of the instabilities can be followed into the highly nonlinear regime, and used to identify the stable, supercritical flow structure at that value of *Re* (which results as the end-product of the instability).

The computing systems division at the IBM Thomas J. Watson Research Center is thanked for access to IBM RS/6000, Model 550 workstations on which the computations in this paper were performed. A. Tomboulides (Princeton University) is thanked for communicating his results to us.

REFERENCES

ACHENBACH, E. 1974 Vortex shedding from spheres. *J. Fluid Mech.* **62**, 209.

CUVELIER, C., SEGAL, A. & STEENHOVEN, A. A. VAN 1986 *Finite Element Methods and Navier–Stokes Equations*. Riedel.

FORNBERG, B. 1988 Steady viscous flow past a sphere at high Reynolds number. *J. Fluid Mech.* **190**, 471.

FORNBERG, B. 1991 Steady incompressible flow past a row of circular cylinders. *J. Fluid Mech.* **225**, 655.

GOLDBURG, A. & FLORSHEIM, B. H. 1966 Transition and Strouhal number for the incompressible wake of various bodies. *Phys. Fluids* **9**, 45.

GRESHO, P. M. 1991 Incompressible fluid dynamics: Some fundamental formulation issues. *Ann. Rev. Fluid Mech.* **23**, 413.

GUNZBURGER, M. D. 1989 *Finite Element Methods for Viscous Incompressible flows*. Academic.

HAGSTROM, T. 1991 Conditions at the downstream boundary for simulations of viscous, incompressible flows. *SIAM J. Sci. Stat. Comput.* **12**, 843.

JACKSON, C. P. 1987 A finite-element study of the onset of vortex shedding in flow past variously shaped bodies. *J. Fluid Mech.* **182**, 23.

KIM, I. & PEARLSTEIN, A. J. 1990 Stability of the flow past a sphere. *J. Fluid Mech.* **211**, 73.

MAGARVEY, R. H. & BISHOP, R. L. 1961*a* Transition ranges for three-dimensional wakes. *Can. J. Phys.* **39**, 1418.

MAGARVEY, R. H. & BISHOP, R. L. 1961*b* Wakes in liquid–liquid systems. *Phys. Fluids* **4**, 800.

MAGARVEY, R. H. & MACLATCHY, C. S. 1965 Vortices in sphere wakes. *Can. J. Phys.* **43**, 1649.

NAKAMURA, I. 1976 Steady wake behind a sphere. *Phys. Fluids* **19**, 5.

NATARAJAN, R. 1992 An Arnoldi-based iteration method for finite element stability problems. *J. Comput. Phys.* **100**, 128.

NATARAJAN, R., FORNBERG, B. & ACRIVOS, A. 1993 Flow past a row of flat plates at large Reynolds number. *Proc. R. Soc. Lond.* A **441**, 211.

PROVANSAL, M., MATHIS, C. & BOYER, L. 1987 Bénard–von Kármán instability: transient and forced regimes. *J. Fluid Mech.* **182**, 1.

ROOS, F. W. & WILLMARTH, W. W. 1971 Some experimental results on sphere and disk drag. *AIAA J.* **9**, 285.

SAAD, Y. 1989 Numerical solution of large nonsymmetric eigenvalue problems. *Comput. Phys. Commun.* **53**, 71.

SAKAMOTO, H. & HANIU, H. 1990 A study of vortex shedding from spheres in a uniform flow. *Trans. ASME* **112**, 386.

STRYKOWSKI, P. J. & SREENIVASAN, K. R. 1990 On the formation and suppression of vortex 'shedding' at low Reynolds numbers. *J. Fluid Mech.* **218**, 71.

TANEDA, S. 1956 Experimental investigation of the wake behind a sphere at low Reynolds numbers. *J. Phys. Soc. Japan* **11**, 1104.

TANEDA, S. 1978 Visual observations of the flow past a sphere at Reynolds numbers between 10^4 and 10^6. *J. Fluid Mech.* **85**, 187.

TOMBOULIDES, A. G. 1993 PhD thesis (in preparation), Department of Applied and Computational Mathematics, Princeton University.

TOMBOULIDES, A. G., ORSZAG, S. A. & KARNIADAKIS, G. E. 1993 Direct and large-eddy simulations of axisymmetric wakes. *AIAA*-93-0546.

WILLMARTH, W. W., HAWK, N. E. & HARVEY, R. L. 1964 Steady and unsteady motions and wakes of freely falling bodies. *Phys. Fluids* **7**, 197.

WINNIKOW, S. & CHAO, B. T. 1966 Droplet motion in purified systems. *Phys. Fluids* **9**, 50.